

GeoLS: an Intensity-based, Geodesic Soft Labeling for Image Segmentation

Sukesh ADIGA VASUDEVA 

ETS Montreal, Canada and Polytechnique Montreal, Canada
MILA-Quebec AI Institute, Montreal, Canada

sukesh.adiga-vasudeva.1@ens.etsmtl.ca

Jose DOLZ 

ETS Montreal, Canada
International Laboratory on Learning Systems (ILLS), Canada

jose.dolz@etsmtl.ca

Herve LOMBAERT

Polytechnique Montreal, Canada and ETS Montreal, Canada
MILA-Quebec AI Institute, Montreal, Canada

herve.lombaert@polymtl.ca

Abstract

1 Soft-label assignments have emerged as prominent strategies in training dense prediction
2 problems, such as image segmentation. These approaches mitigate the limitations of hard
3 labels, such as inter-class relationships in the data and spatial relationships between a
4 given pixel and its neighbors. Nevertheless, most existing methods rely only on ground-
5 truth masks and ignore the underlying image context associated with each label. For
6 instance, image intensities convey information that could potentially clear ambiguities in
7 the annotation. This paper, therefore, proposes a Geodesic Label Smoothing (GeoLS)
8 approach that incorporates image intensity information within the soft labeling process.
9 Specifically, we leverage the geodesic distance transform to capture the intensity variations
10 between pixels. The generated maps geodesically modify the hard labels to obtain new
11 intensity-based soft labels. The resulting geodesic soft labels better model spatial and
12 class-wise relationships as they capture the variations of image gradients across classes
13 and anatomy. The benefits of our intensity-based geodesic soft labels are assessed on
14 three diverse sets of publicly accessible segmentation datasets. Our experimental results
15 show that the proposed method consistently improves the segmentation accuracy compared
16 to state-of-the-art soft-labeling techniques in terms of the Dice similarity and Hausdorff
17 distance.

18 **Keywords:** Geodesic Distance, Soft Labeling, Label Smoothing, Image Segmentation.

19 1. Introduction

20 Image segmentation is a highly structured and dense prediction problem where pixels in an
21 image are grouped into a set of target regions, such as organs or tumors (Pham et al., 2000;
22 Suetens, 2017). It plays a pivotal role in clinical decision systems, notably in computer-
23 assisted prognosis and diagnosis, treatment planning, and intervention support (Duncan
24 and Ayache, 2000; Zhou et al., 2019). Recent advancements in segmentation methods are
25 primarily due to the ability of deep learning techniques to solve such complex predictive
26 tasks (Litjens et al., 2017; Hesamian et al., 2019). Training these approaches involves min-
27 imizing the deviation of the network predictions from the given ground-truth annotations

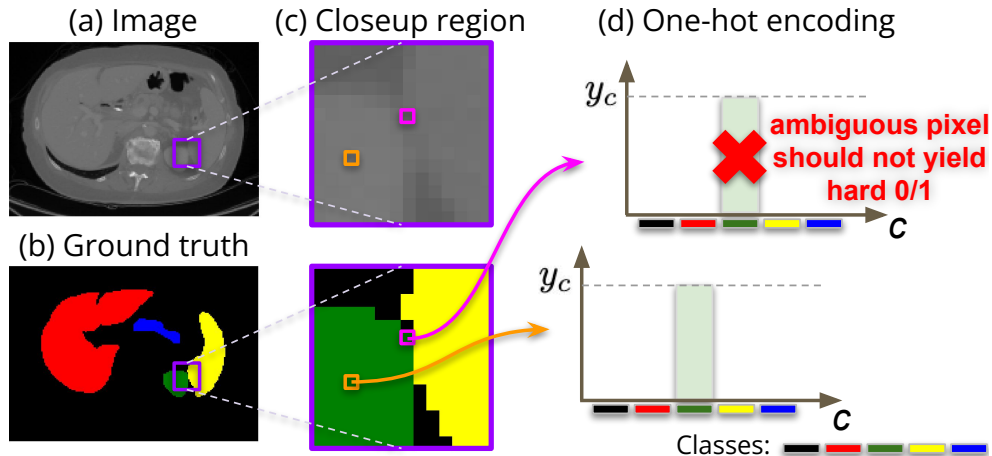


Figure 1: **Limitation of one-hot label assignments.** (a) A sample image and (b) its corresponding ground-truth mask, (c) a closeup image around the boundary region (purple), and (d) the one-hot (OH) encoding for two pixels (orange and pink in closeup images). The OH encoding of a pixel (orange) inside the kidney region (green label) may represent the true class distribution (y_c) since the label is spatially consistent with neighboring pixels. Conversely, the OH label assignment of a pixel (pink) near the boundary region may not reflect the true class distribution as it does not capture the underlying spatial ambiguities in the image. Different colors denote the class labels c .

28 using various objective functions (Rubinstein and Kroese, 2004; Sudre et al., 2017; Lin et al.,
 29 2017).

30 A common strategy to measure this deviation is to employ the cross-entropy function
 31 with the ground-truth mask represented as one-hot encoded vectors. This learning ob-
 32 jective exhibits remarkable performance in problems needing predictions of independent
 33 classes, such as in whole-image classification (Baum and Wilczek, 1987; He et al., 2016;
 34 Szegedy et al., 2017). Nevertheless, the use of standard one-hot encoding in segmentation
 35 tasks can be sub-optimal since class predictions at each pixel are inherently conditioned with
 36 surrounding pixels. Such encoding indeed fails to capture the spatial relationships across
 37 neighborhoods as well as inter-class relationships within an image. These relationships,
 38 however, are crucial for the segmentation of medical images. For instance, labels can be
 39 similar for pixels within a homogeneous region, but vary near object boundaries due to var-
 40 ious image ambiguities (Fig. 1). Such ambiguity can be attributed to partial volume effect,
 41 motion artifacts, or image acquisition, among other reasons. Moreover, the one-hot label
 42 assignments are solely based on the provided ground-truth masks, where the underlying
 43 spatial and inter-class relationships are disregarded. Therefore, explicitly modeling spatial
 44 and inter-class relationships in the label assignments is sought to improve the performance
 45 of the segmentation model.

46 Recent attempts to incorporate the inter-class relationships in the labels (Szegedy et al.,
 47 2016; Galdran et al., 2020) generally modify the hard one-hot encoding into a softer version.
 48 For instance, Label Smoothing (LS) (Szegedy et al., 2016) uniformly redistributes a portion
 49 of the target-class probability into all non-target classes to obtain a new soft label assignment

50 for training a deep model. In (Galdran et al., 2020), a non-uniform label smoothing approach
 51 is proposed to capture the underlying structure within annotations. This method uses a
 52 Gaussian smoothing on each target class to redistribute probability over other classes. It
 53 is particularly suitable for datasets featuring ordered class labels, such as tumor or disease
 54 grading. These label-smoothing approaches, however, disregard the spatial relationships in
 55 their soft-label assignments.

56 To capture the spatial relationships, a few approaches alter the target segmentation mask
 57 to obtain softer labels in the boundary regions (Kats et al., 2019; Gros et al., 2021). For
 58 instance, Kats et al. (2019) generates the soft labels in the dilated regions of the target masks
 59 by adding granularity in the object boundaries. Furthermore, a Spatially-Varying Label
 60 Smoothing (SVLS) approach models the annotation ambiguity around object boundaries in
 61 target masks (Islam and Glocker, 2021). Its soft labels capture the local structural variations
 62 by applying a Gaussian-smoothing operation on the target masks. However, the annotation
 63 ambiguities of object boundaries stem from poorly defined image intensities caused by
 64 imaging techniques or existing pathologies, which inherently leads to labeling inaccuracies
 65 (Joskowicz et al., 2019; Hayward et al., 2008). These ambiguities are not captured in these
 66 soft-labeling methods, as they solely rely on the given ground-truth masks.

67 One solution is to incorporate image-based metrics in the soft-label assignments process.
 68 More specifically, a geodesic distance transform captures intensity variations and spatial
 69 distances within an image (Toivanen, 1996; Criminisi et al., 2008). Our approach, therefore,
 70 leverages the geodesic distance in order to capture inter-pixel and inter-class relationships
 71 during the label smoothing process. The generated soft labels thus become intensity-aware,
 72 capturing image gradient information across object boundaries. Incorporating our geodesic
 73 soft labels in model training is found to improve the segmentation performance, as they
 74 model the underlying intensity variations across objects and labels.

75 **Our contributions:** This work introduces a novel Geodesic Label Smoothing (GeoLS)
 76 approach to enhance image segmentation. Specifically, our originality lies in leveraging the
 77 geodesic distance transform to embed intensity variations in the soft-labeling process. Un-
 78 like existing soft-labeling strategies, our proposed method utilizes geodesic maps to smooth
 79 the hard labels, thus capturing the essential intensity information that is crucial for medical
 80 image segmentation. The resulting intensity-based soft labels capture class-wise relation-
 81 ships by considering image gradient information between two or more object categories.
 82 Furthermore, the geodesic distance between pixels captures the spatial relationships, inte-
 83 grating richer information than the Euclidean distance. Our GeoLS method is extensively
 84 validated across three distinct medical image segmentation benchmarks: the brain tumor
 85 dataset (Bakas et al., 2017, 2018), the abdominal organ dataset (Ma et al., 2022), and the
 86 prostatic zone dataset (Litjens et al., 2014). The findings in our experiments demonstrate
 87 the merit of GeoLS over existing soft-labeling methods.

88 This manuscript provides a significant extension upon our preliminary work (Adiga Va-
 89 sudeva et al., 2023). Specifically, we conduct exhaustive experiments on a variety of datasets
 90 with thorough analyses to demonstrate the performance of our geodesic approach. Notably,
 91 our method is evaluated on a diversity of segmentation datasets, including tumors in brain
 92 MRIs (BraTS), multi-organs in abdominal CT scans (FLARE), and multiple zones in pro-
 93 static MRIs (ProstateX). Moreover, our experiments include comprehensive ablation studies

94 to further highlight the effectiveness of our geodesic soft labels for image segmentation. In
 95 particular, we investigate the parameters influencing the generation of geodesic soft labels,
 96 such as studying the impact of intensity variation and different seeding strategies in obtain-
 97 ing our soft labels. Additionally, we conduct experiments focusing on the combination of
 98 our proposed loss with a Dice loss, a boundary loss, and a focal loss, which aim to assess
 99 the synergies in combining these approaches.

100 2. Related Work

101 2.1 Soft labeling

102 Soft labeling has been actively investigated in the machine learning community (Szegedy
 103 et al., 2016; Müller et al., 2019; Zhang et al., 2021). The early methods often leverage the
 104 nearest-neighbor points to obtain a soft label (Keller et al., 1985; Seo et al., 2003). Such a
 105 labeling scheme captures multiple class characteristics in the dataset, which are later used
 106 to train a classifier (El Gayar et al., 2006). More recently, Szegedy et al. (2016) proposed
 107 a label smoothing strategy for training deep neural networks. This smoothing strategy
 108 uniformly redistributes the portion of the one-hot label of a given class to all other classes.
 109 The model trained with these soft labels has been shown to improve the performance in
 110 classification tasks in both computer vision (Szegedy et al., 2016; Müller et al., 2019) and
 111 medical imaging domains (Galdran et al., 2020; He et al., 2020; Islam et al., 2020). It is
 112 also shown to be effective in handling noisy labels (Lukasik et al., 2020; Lukov et al., 2022).

113 In the context of image segmentation tasks, the label smoothing strategy (Szegedy et al.,
 114 2016) captures inter-class relationships within an image. However, It is also essential to con-
 115 sider the spatial relationships within neighboring regions. Recent approaches (Kats et al.,
 116 2019; Gros et al., 2021; Islam and Glocker, 2021) attempt to capture such relationships
 117 with spatially-varying smooth labels, improving segmentation performance. For instance,
 118 Kats et al. (2019) obtains soft labels by expanding the original binary mask using a dilation
 119 operation and subsequently assigns a soft value in the extended region. In (Gros et al.,
 120 2021), non-binary pre-processing and data augmentation techniques are employed on the
 121 target mask to obtain soft labels around the boundaries. These strategies are designed for
 122 binary segmentation tasks, where they disregard the probability distribution in the label
 123 assignments. Therefore, adopting them directly to multi-class segmentation is not trivial.
 124 A SVLS approach generates the soft labels by redistributing the class probabilities based
 125 on Gaussian filtering (Islam and Glocker, 2021). Nevertheless, these soft-labeling methods
 126 are entirely based on ground-truth masks while ignoring the ambiguities arising from im-
 127 age intensities. Alternately, soft labels can also be generated using multi-rater annotations
 128 (Lourenço-Silva and Oliveira, 2021). Although having multiple annotations for soft labels is
 129 ideal, it is even more expensive to obtain in practice since it requires multiple independent
 130 annotators. Furthermore, a few methods also utilize uncertainty maps for soft segmenta-
 131 tion (Tang et al., 2022; Wang et al., 2023). Nevertheless, these methods require multiple
 132 segmentation predictions to compute uncertainty maps, which are computationally expen-
 133 sive. Compared to these approaches, our method leverages the geodesic distance transform
 134 (Toivanen, 1996) to capture the intensity variations in the label smoothing process. The
 135 resulting intensity-based soft labels capture spatial and class-wise relationships through the
 136 geodesic maps. Moreover, the generated soft labels are computed once and incorporated

137 into the learning objective to train a segmentation model. Also, our method generates new
 138 soft labels from a single annotation and can be seamlessly integrated into the segmentation
 139 network.

140 2.2 Geodesic Distance Transform (GDT)

141 The GDT is commonly used for smooth and contrast-sensitive image segmentation (Criminisi et al., 2008; Protiere and Sapiro, 2007; Toivanen, 1996), as it captures the local
 142 contrast and structural information within an image. The seminal work, GeoS (Criminisi et al., 2008), proposes a generalized geodesic distance (GGD) method for segmentation
 143 tasks in an energy-based model. The effectiveness of GeoS has led to various segmentation
 144 approaches (Kontschieder et al., 2013; Wang et al., 2014; Qiu et al., 2015). For instance,
 145 Wang et al. (2014) utilizes GGDs to bring the spatial context between object boundaries
 146 in an atlas-based label propagation method. Recent approaches have leveraged GGDs in
 147 deep learning techniques to improve image segmentation (Wang et al., 2018; Bui et al.,
 148 2019; Hammoumi et al., 2021; Wei et al., 2022). For instance, Bui et al. (2019) proposes
 149 a regression of the geodesic distance maps to regularize the segmentation network through
 150 an additional prediction branch. Similarly, Ying et al. (2023) regularizes geodesic distance
 151 maps in a dual-branch network to enhance edge details for weakly supervised segmentation.
 152 To improve initial segmentation, the geodesic distance from user interactions (Wang et al.,
 153 2018) or initial network predictions (Wei et al., 2022) are employed to provide the contex-
 154 tual information. The resulting geodesic maps are subsequently used as additional inputs
 155 to the refinement network. These existing approaches require an extra prediction branch or
 156 refinement network to integrate the geodesic maps. In contrast, our method leverages the
 157 geodesic distance to embed underlying image context information into the label smoothing
 158 process. The generated soft labels are computed once and consequently incorporated into
 159 the learning objective to train the segmentation model. Our geodesic soft-labels, therefore,
 160 can be directly plugged into any segmentation network.
 161
 162

163 3. Method

164 An outline of the proposed approach comparing hard labels (OH) and existing soft labels
 165 (LS and SVLS) is shown in Fig. 2. Consider two closeup regions with the same masks
 166 but differing image intensities as in Fig. 2. The existing methods rely only on ground-
 167 truth masks to generate the soft labels. Therefore, they have the same class probability
 168 maps in both closeup regions. In contrast, our approach adds image context by leveraging
 169 geodesic distance transform in the soft-labeling process. The resulting intensity-based soft
 170 labels capture the underlying image ambiguities through geodesic maps. Thus, our method
 171 produces different class probability maps in the two closeups. The following subsections
 172 describe the label smoothing formulation and proposed geodesic soft-labeling process.

173 3.1 Preliminaries

174 Let $\{(x_i, y_i)\}_{i=1}^N$ indicate the training dataset with N samples, where $x_i \in \mathbb{R}^{S \times H \times W}$ repre-
 175 sents a 3D input volume of size $S \times H \times W$, and $y_i \in \{0, 1\}^{C \times S \times H \times W}$ denotes the corre-
 176 sponding ground truth in OH representation with C number of classes. The Cross-Entropy

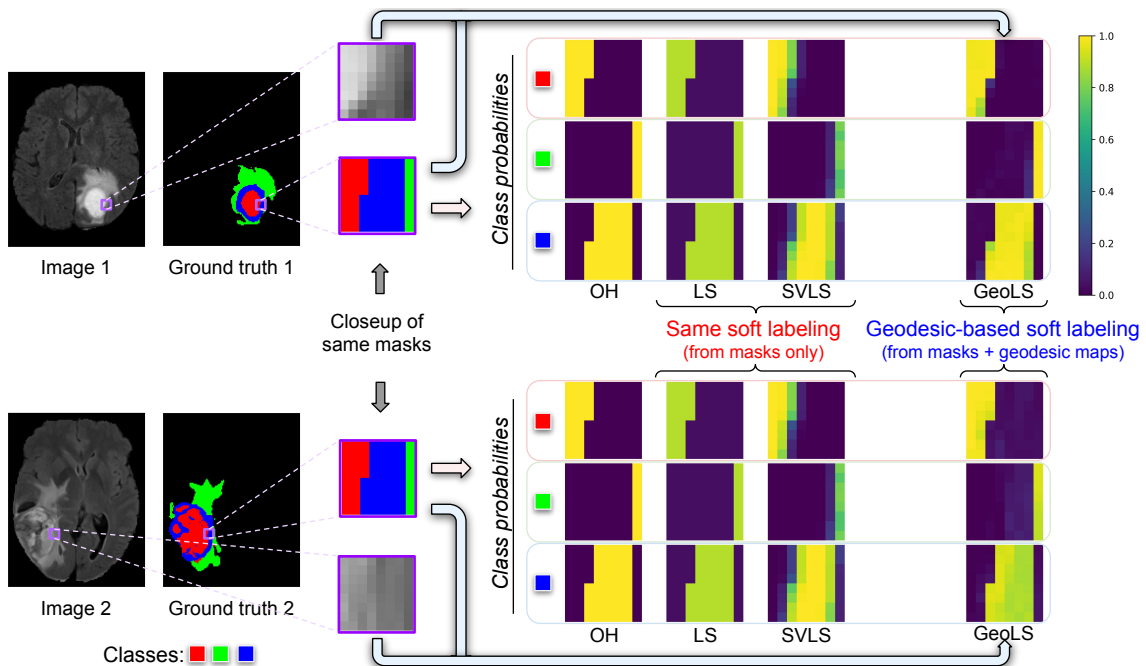


Figure 2: **Visualization of different soft labelings.** Left side: Two samples, their corresponding ground-truth masks, and closeup images having the same ground-truth masks around tumor regions. Right side: The probabilities of each class (in red, blue, and green colors) for the same closeup images from One-Hot (OH) encoding, Label Smoothing (LS), Spatially-Varying LS (SVLS), and ours (GeoLS). Since OH, LS, and SVLS are solely obtained from ground-truth masks, they have the same class probabilities maps for both closeup regions (compare top vs bottom). In contrast, our proposed method employs geodesic maps to smooth the hard labels, thus capturing intensity variations across object boundaries. Best viewed in color.

177 (CE) loss function for a given voxel is defined as:

$$\mathcal{L}_{CE} = - \sum_{c=1}^C y_c \log(p_c), \quad (1)$$

178 where p_c is the predicted softmax probability from the segmentation network. For simplicity,
 179 we use i and c notations wherever necessary and assume that the cardinality of the training
 180 set normalizes the loss function.

181 The OH label encoding, y_c , assigns a probability of ‘1’ for the target class and ‘0’ for the
 182 non-target classes. Such assignments fail to provide the model with annotation ambiguity
 183 since they do not capture the underlying inter-class relationships within the image. One
 184 way to model these relationships is by softening the hard OH encoding during the training
 185 process. For instance, the LS method (Szegedy et al., 2016) reduces the probability of the
 186 target class by a factor α and evenly distributes it across all classes. The resulting soft label
 187 for a given voxel is:

$$y_c^{LS} = (1 - \alpha)y_c + \frac{\alpha}{C} \quad (2)$$

188 These soft labels are subsequently used in training a segmentation network by replacing
 189 the original OH label in Eq 1. This strategy has been shown to improve performance in
 190 classification tasks (Szegedy et al., 2016; He et al., 2020; Islam et al., 2020). Nevertheless,
 191 LS ignores the intrinsic spatial structure that is essential for the segmentation tasks.

192 3.2 Geodesic Label Smoothing (GeoLS)

193 Existing soft-labeling approaches modify the segmentation masks to capture the spatial
 194 relationships (Kats et al., 2019; Gros et al., 2021; Islam and Glocker, 2021), thereby ac-
 195 counting for the annotation ambiguities around the object boundaries. Nevertheless, they
 196 largely overlook the annotation ambiguities coming from the image intensities, being prone
 197 to annotation mistakes. To consider such image ambiguities, we integrate the geodesic
 198 distance transform (Toivanen, 1996) directly in the soft labeling of pixels. This addition
 199 captures the intensity variations as well as the spatial distance between pixels in an image.
 200 The following subsections elaborate on our geodesic label-smoothing method.

201 3.2.1 GENERALIZED GEODESIC DISTANCE (GGD) TRANSFORM

202 The GGD transform (Criminisi et al., 2008) computes the shortest geodesic distance between
 203 a set of reference points, known as seed points, and each pixel in an image. This transform
 204 produces a distance map derived from a spatial distance and image gradient combination.
 205 The seed points can be either a single point or a set of points selected from the object of
 206 interest. Let \mathcal{S}_c represent a set of seed points upon the target class c . The generalized
 207 geodesic distance of each voxel v to the set \mathcal{S}_c of a target class is described as:

$$D_c(v; \mathcal{S}_c, x_i) = \min_{v' \in \mathcal{S}_c} d(v, v', x_i), \quad (3)$$

208 with:

$$d(v, v', x_i) = \min_{\mathbf{p} \in P_{v, v'}} \int \sqrt{\|\mathbf{p}'(s)\|^2 + \gamma^2(\nabla x_i \cdot \mathbf{u}(s))^2} ds, \quad (4)$$

209 where $P_{v, v'}$ represents the set of all paths between voxels v and v' , and $\mathbf{p}(s)$ denotes one
 210 such path parameterized by $s \in [0, 1]$. We define a unit vector $\mathbf{u}(s) = \frac{\mathbf{p}'(s)}{\|\mathbf{p}'(s)\|}$, which is
 211 tangent in the direction of the path, and whose spatial derivative is $\mathbf{p}'(s) = \frac{\partial \mathbf{p}(s)}{\partial s}$.

212 In Eq. 4, the first term, $\mathbf{p}'(s)$, accounts for the Euclidean distance, while the second term
 213 captures the image gradient information (∇x_i). The parameter γ , termed the geodesic fac-
 214 tor, balances the contribution of the image gradient, and the Euclidean distance between
 215 the seed set \mathcal{S}_c and each voxel in the image. When $\gamma = 0$, Eq. 4 simplifies to the Euclidean
 216 Distance, whereas setting γ to 1 facilitates computation of the geodesic distance as de-
 217 scribed in (Criminisi et al., 2008). In practice, the geodesic distance transform is optimally
 218 estimated using the raster scan algorithm (Toivanen, 1996; Criminisi et al., 2008).

219 An example of generating a geodesic map is shown in Fig. 3. The seed points are chosen
 220 by the skeletonization operation on a target mask. The GGD map is subsequently obtained

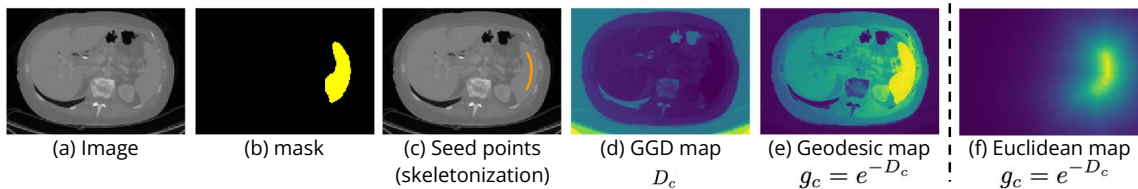


Figure 3: **Geodesic map generation.** (a) A sample image and (b) a corresponding segmentation mask of a spleen organ. (c) Seed points (orange, overlaid on the image) are derived by skeletonization of the segmentation mask. (d) The GGD map is generated from seed sets to each pixel in the image. (e) Our final geodesic map is obtained by inverting the GGD map. (f) An Euclidean map is similarly obtained for the same seed points. Notice that the Euclidean map spreads uniformly from seed points in all directions. Whereas our geodesic map spreads based on both spatial distance and gradient information, capturing the underlying intensity similarities.

221 using Eq. 4. To highlight the object of interest, we invert the GGD map to get the final
 222 geodesic map for each target class as follows:

$$g_c = e^{-D_c} \quad (5)$$

223 The resulting maps are thus in the range $[0, 1]$. The geodesic map of the background class
 224 is obtained by inverting the average of foreground geodesic maps, also in the range $[0, 1]$. In
 225 Fig. 3, we have also added an Euclidean distance map for comparison with a geodesic map.
 226 The Euclidean map spreads uniformly from seed points in all directions. In contrast, our
 227 geodesic map propagates based on both spatial distance and gradient information, capturing
 228 the underlying intensity similarities.

229 3.2.2 GEODESIC SOFT LABELS

230 The geodesic maps encode image gradient details as a function of distance from the target
 231 objects. Such maps account for the intensity variations across object boundaries. Our
 232 approach, therefore, avails the geodesic maps for smoothing the hard labels. In order to
 233 accomplish this, we first normalize the geodesic map of each class as $\tilde{g}_c = \frac{g_c}{\sum_c g_c}$, such
 234 that it follows a probability distribution. Subsequently, the normalized geodesic maps are
 235 integrated with the original one-hot encoding to produce the new intensity-based soft labels,
 236 as defined below:

$$y_c^{GeoLS} = (1 - \alpha)y_c + \alpha\tilde{g}_c \quad (6)$$

237 These generated soft labels are thereafter substituted in Eq. 1 to facilitate the train-
 238 ing of the segmentation network. The generation of our proposed geodesic soft labels is
 239 demonstrated in Fig 4. As our approach incorporates intensity variations into the target
 240 label assignments through geodesic maps, it effectively guides the network toward better
 241 segmentation.

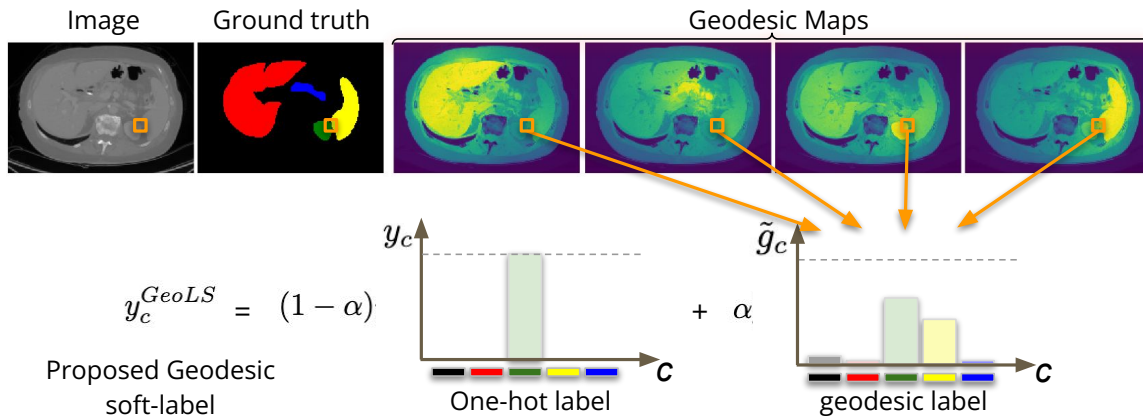


Figure 4: **Illustration of our proposed Geodesic Label Smoothing (GeoLS)**. The geodesic maps for all target labels are combined to form a probability distribution. The generated geodesic label is subsequently used to modify the one-hot encoding to obtain the proposed intensity-based soft label. Our soft label captures the underlying intensity variation, thus it can better guide the segmentation network in ambiguous regions.

242 4. Experiments and Results

243 4.1 Datasets

244 In order to validate our geodesic label-smoothing method, we utilize three publicly accessible
 245 segmentation datasets. These datasets include: a) the Brain Tumor Segmentation dataset
 246 obtained from the 2019 BraTS challenge (Bakas et al., 2017, 2018), b) the multi-organ
 247 abdominal segmentation dataset from the 2021 FLARE challenge (Ma et al., 2022), and c)
 248 the prostatic zone segmentation dataset from the ProstateX challenge (Litjens et al., 2014).
 249 A detailed description of these datasets and our experimental settings are presented next.

250 **a) BraTS:** This dataset comprises 335 multimodal MRI volumes of the brain, containing
 251 T1, T2, FLAIR, and T1ce sequences. These volumes are preprocessed with skull-stripped,
 252 co-registered to a fixed template, and resampled to an isotropic resolution of 1 mm^3 . The
 253 dataset contains corresponding annotations of glioma tumors, including delineations of the
 254 necrotic and non-enhancing core, edema, and enhancing tumor regions. These regions are
 255 converted into Whole Tumor (WT), Tumor Core (TC), and Enhancing Tumor (ET) for
 256 evaluation purposes. The dataset is partitioned into 235 for training, 32 for validation, and
 257 68 for testing across all our experiments.

258 **b) FLARE:** The dataset consists of 361 CT volumes of abdominal regions with seg-
 259 mentation masks of four organs: liver, kidney, spleen, and pancreas. These volumes have
 260 variable resolutions, which are standardized by resampling to a consistent resolution of
 261 $2 \times 2 \times 2.5 \text{ mm}^3$. Subsequently, they are intensity normalized by retaining values within
 262 the percentile range of $[0.5, 0.95]$, as followed in the literature (Isensee et al., 2021). We
 263 employ a predefined dataset split for all experiments, allocating 260 volumes for training,
 264 26 for validation, and the remaining 75 for testing.

265 **c) ProstateX:** The dataset includes 98 prostatic T2 MRI scans and corresponding seg-
 266 mentation labels of four anatomical zones, including the peripheral zone (PZ), transition
 267 zone (TZ), distal prostatic urethra (DPU), and anterior fibromuscular stroma (AFS). All
 268 volumes are resampled into a fixed resolution of $3 \times 0.5 \times 0.5 \text{ mm}^3$ as followed in (Islam
 269 and Glocker, 2021). For all our experiments, the dataset is split into 68 for training, 10 for
 270 validation, and the remaining 20 for testing.

271 4.2 Training and implementation details.

272 To assess the contribution of our geodesic soft labeling, we utilize a 3D U-net (Çiçek et al.,
 273 2016) architecture for the segmentation network. This model is trained using Adam opti-
 274 mizer (Kingma and Ba, 2015) with a learning rate of 10^{-4} and weight decay of 10^{-4} . The
 275 input size of $128 \times 192 \times 192$ in BraTS, $112 \times 160 \times 208$ in FLARE, and $24 \times 320 \times 320$
 276 in ProstateX experiments are fed into the network. The data augmentations such as ran-
 277 dom flipping and rotation are utilized, as in (Islam and Glocker, 2021). The network is
 278 trained for 200 epochs with a batch size of 4. For inference, the model with the best dice
 279 score on the validation set is selected for testing. Our evaluation includes experiments
 280 with CE, Focal Loss (FL) (Lin et al., 2017), LS (Szegedy et al., 2016), and SVLS (Islam
 281 and Glocker, 2021) losses as training objectives. Following the literature, commonly uti-
 282 lized hyperparameter values are considered for each baseline approach, and the result is
 283 reported for a value with the best dice score on the validation set. In particular, the fo-
 284 cusing parameter γ in FL is set to $\{1, 2, 3\}$. In the case of LS, $\alpha \in \{0.1, 0.2, 0.3\}$ are used,
 285 whereas $\sigma \in \{0.5, 1, 2\}$ values are employed in SVLS with a kernel size of 3. In our method,
 286 the geodesic factor γ is explored for $\{0.5, 0.75, 1\}$ values with a fixed smoothing factor of
 287 $\alpha = 0.1$. To obtain the geodesic maps, an open-source library, *GeodisTK*¹, is employed
 288 with a skeletonization of a segmentation mask as seed points. Note that our soft labels are
 289 computed offline, requiring virtually no additional computation during the training process.
 290 The only additional cost is loading the geodesic maps, whose computational burden is neg-
 291 ligible. The geodesic maps are not needed during the inference step, resulting in exactly
 292 the same computation cost as existing approaches. All our experiments were executed on
 293 an NVIDIA RTX A6000 GPU with PyTorch 1.8.0. Our GeoLS implementation is available
 294 at: <https://github.com/adigas/GeoLS>.

295 4.3 Evaluation Metrics

296 The segmentation performance is evaluated with standard and widely used evaluation mea-
 297 sures, such as the Dice Similarity Coefficient (DSC) and the 95% Hausdorff Distance (HD).
 298 The former measure estimates the overlap between ground truth labels and predictions,
 299 whereas the latter measures the distance between ground truth and predicted segmentation
 300 boundaries. To ensure a fair comparison, we conducted all experiments three times with
 301 fixed seed sets on identical machines, presenting results with mean and standard deviation
 302 values.

1. <https://github.com/taigw/GeodisTK>

303 **4.4 Comparison with the state-of-the-art**

304 The performance of the proposed geodesic soft-labeling approach is first compared with
 305 CE, FL, and state-of-the-art soft-labeling methods (LS (Szegedy et al., 2016) and SVLS
 306 (Islam and Glocker, 2021)), and their discriminative results are reported in Tables 1-3 for
 307 all three datasets. The table also includes the hyperparameter value corresponding to the
 308 best-performing model for each method.

309 The performance of various methods on multi-class brain tumor segmentation dataset
 310 is shown in Table 1. The results show that employing soft labels improves the segmen-
 311 tation performance compared to models trained with a CE loss on hard labels in both
 312 scores. Among soft-labeling baselines, FL and SVLS achieve the best DSC and HD scores,
 313 respectively. Our approach outperforms these best-performing baselines in both DSC and
 314 HD scores in all tumor categories. Notably, we observe that the proposed GeoLS indeed
 315 benefits in the enhancing tumor (ET) region. Such a region is often irregular and poorly
 316 defined, which leads to imprecise annotation (Menze et al., 2014). Our method improves
 317 this challenging region by 1.06% in DSC score and 0.45 mm in HD, highlighting the advan-
 318 tage of combining the intensity information in our soft labels. These results demonstrate
 319 the merit of using our geodesic soft-labeling over hard-labeling and existing soft-labeling
 320 approaches.

321 Table 2 presents the results of the multi-organ abdominal segmentation on the FLARE
 322 test set. A similar pattern is observable in the LS, SVLS, and GeoLS results compared to
 323 those obtained from the BraTS dataset (Table 1). Nevertheless, there is an apparent per-
 324 formance gap in FL compared to CE results, which may be attributed to the over-emphasis
 325 on mislabeled pixels present in the data. Overall, our GeoLS yields the best segmentation
 326 performance corresponding to the baselines, notably enhancing the segmentation in the
 327 challenging pancreas and spleen regions.

328 The results of the multi-class prostatic zone segmentation on the ProstateX dataset are
 329 reported in Table 3. A similar trend in FL, LS, and GeoLS results is observed as in Table 1.
 330 However, SVLS produces a drop in performance compared to CE results (HD), possibly
 331 due to the over-suppression of original one-hot encoding in the boundaries. Moreover,

Table 1: **Segmentation results on the BraTS test set.** In all tumor structures (ET, TC, WT), our method yields the best DSC and HD scores. For each tumor structure, bold and underlined indicate the best and second-best methods.

	Methods	ET	TC	WT	Average
DSC (%) ↑	CE	72.05 ± 2.14	82.38 ± 0.91	90.09 ± 0.39	81.51 ± 1.03
	FL ($\gamma = 1$)	<u>73.55 ± 0.49</u>	<u>82.82 ± 0.20</u>	90.37 ± 0.16	<u>82.25 ± 0.20</u>
	LS ($\alpha = 0.1$)	<u>73.28 ± 0.85</u>	<u>82.65 ± 0.30</u>	<u>90.46 ± 0.08</u>	<u>82.13 ± 0.35</u>
	SVLS ($\sigma = 1.0$)	73.15 ± 2.82	82.67 ± 1.96	<u>90.43 ± 0.78</u>	82.08 ± 1.81
	Ours ($\gamma = 0.75$)	<u>74.61 ± 0.79</u>	<u>83.51 ± 0.24</u>	<u>90.88 ± 0.12</u>	<u>83.00 ± 0.31</u>
HD (mm) ↓	CE	14.55 ± 1.61	7.64 ± 1.15	6.28 ± 0.86	9.49 ± 1.20
	FL ($\gamma = 1$)	<u>12.81 ± 1.11</u>	7.31 ± 0.32	5.96 ± 0.18	8.69 ± 0.31
	LS ($\alpha = 0.1$)	<u>13.52 ± 0.35</u>	7.23 ± 0.16	5.95 ± 0.16	8.90 ± 0.21
	SVLS ($\sigma = 1.0$)	12.83 ± 2.70	<u>6.93 ± 1.37</u>	<u>5.72 ± 1.10</u>	<u>8.50 ± 1.70</u>
	Ours ($\gamma = 0.75$)	<u>12.36 ± 0.56</u>	<u>6.08 ± 0.61</u>	<u>5.22 ± 0.52</u>	<u>7.89 ± 0.32</u>

Table 2: **Segmentation results on the FLARE test set.** Our method produces the best DSC and HD scores on average results as well as on a challenging pancreas organ. For each abdominal organ, bold and underlined indicate the best and second-best methods.

	Methods	Liver	Kidney	Spleen	Pancreas	Average
DSC (%) ↑	CE	94.88 ± 0.31	94.70 ± 0.33	95.46 ± 0.85	72.52 ± 0.61	89.39 ± 0.14
	FL ($\gamma = 1$)	94.84 ± 1.08	94.38 ± 0.35	95.56 ± 0.72	69.66 ± 2.02	88.61 ± 0.90
	LS ($\alpha = 0.1$)	95.96 ± 1.11	94.89 ± 0.35	<u>95.61 ± 0.63</u>	73.07 ± 1.35	<u>89.88 ± 0.38</u>
	SVLS ($\sigma = 0.5$)	<u>95.76 ± 0.34</u>	94.28 ± 0.34	95.01 ± 0.09	<u>73.39 ± 0.16</u>	89.61 ± 0.10
	Ours ($\gamma = 1.0$)	<u>95.60 ± 0.87</u>	<u>94.80 ± 0.37</u>	96.52 ± 0.30	73.72 ± 1.02	90.16 ± 0.44
HD (mm) ↓	CE	4.15 ± 1.10	2.94 ± 0.11	2.98 ± 1.06	6.72 ± 1.18	4.20 ± 0.19
	FL ($\gamma = 1$)	3.28 ± 1.28	3.22 ± 0.32	2.80 ± 1.08	8.03 ± 0.46	4.33 ± 0.61
	LS ($\alpha = 0.1$)	<u>2.87 ± 1.14</u>	<u>2.93 ± 0.37</u>	2.60 ± 0.24	6.37 ± 1.03	3.69 ± 0.26
	SVLS ($\sigma = 0.5$)	2.61 ± 1.06	3.17 ± 0.78	1.42 ± 0.18	<u>6.26 ± 0.48</u>	3.36 ± 0.20
	Ours ($\gamma = 1.0$)	3.01 ± 1.05	2.40 ± 0.50	<u>1.49 ± 0.55</u>	5.59 ± 0.20	3.12 ± 0.21

Table 3: **Segmentation results on the ProstateX test set.** Our method is competitive in most cases and achieves the best DSC score on average results. At the same time, baselines are ranked differently across prostatic zones (PZ, TZ, DPU, and AFS). For each prostatic zone, bold and underlined indicate the best and second-best methods.

	Methods	PZ	TZ	DPU	AFS	Average
DSC (%) ↑	CE	71.56 ± 0.55	86.34 ± 0.28	48.39 ± 2.46	38.27 ± 4.46	61.14 ± 1.21
	FL ($\gamma = 1$)	72.18 ± 1.11	<u>86.38 ± 0.20</u>	51.19 ± 2.73	35.50 ± 6.85	61.31 ± 1.96
	LS ($\alpha = 0.2$)	70.52 ± 0.31	86.34 ± 0.46	53.31 ± 2.89	35.16 ± 6.65	<u>61.33 ± 1.29</u>
	SVLS ($\sigma = 1.0$)	<u>72.08 ± 1.89</u>	85.89 ± 0.64	51.10 ± 4.14	35.67 ± 3.08	61.19 ± 2.12
	Ours ($\gamma = 1.0$)	<u>70.86 ± 1.11</u>	86.51 ± 0.36	<u>51.50 ± 0.50</u>	39.50 ± 2.60	62.09 ± 0.75
HD (mm) ↓	CE	6.51 ± 0.34	3.22 ± 0.10	11.28 ± 0.44	9.58 ± 1.21	7.65 ± 0.24
	FL ($\gamma = 1$)	5.76 ± 0.97	3.38 ± 0.39	7.89 ± 3.34	<u>9.68 ± 0.59</u>	6.68 ± 1.05
	LS ($\alpha = 0.2$)	6.64 ± 0.69	<u>3.33 ± 0.15</u>	7.28 ± 2.20	9.75 ± 1.14	6.75 ± 0.70
	SVLS ($\sigma = 1.0$)	7.04 ± 0.84	3.73 ± 0.24	<u>10.94 ± 5.75</u>	10.2 ± 1.26	<u>7.98 ± 1.59</u>
	Ours ($\gamma = 1.0$)	7.83 ± 2.72	3.22 ± 0.06	6.50 ± 0.52	9.78 ± 0.26	6.83 ± 0.78

332 existing methods are ranked differently across datasets and evaluation measures, indicating
 333 that these approaches are sensitive to datasets. In contrast, our GeoLS outperforms the
 334 state-of-the-art approaches in most cases. Based on these results, we can conclude that
 335 our method remains consistent across diverse datasets, highlighting the robustness of our
 336 intensity-based soft labels.

337 4.5 Qualitative Results

338 Figure 5 shows the visual comparison of different segmentation results on brain tumors from
 339 BraTS, abdominal organs from FLARE, and prostatic zones from ProstateX datasets. In
 340 brain tumor segmentations (top row), the results of existing approaches (OH, FL, SVLS) are
 341 predominantly over-segmenting in non-enhancing core regions (blue), whereas the LS and
 342 GeoLS reduce the segmentation errors. In the middle row of Fig. 5, the existing methods
 343 struggle to segment the challenging pancreas organ (yellow) organ. In contrast to these base-
 344 lines, our GeoLS delivers a superior segmentation of the pancreas organ. The prostatic zone

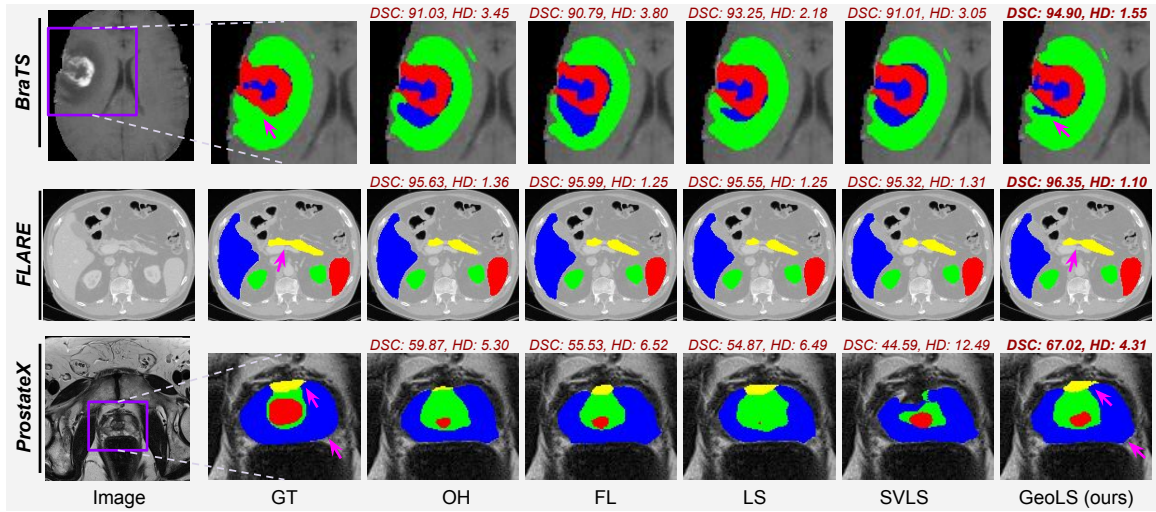


Figure 5: **Qualitative results across BraTS (top), FLARE (middle), and ProstateX (bottom) datasets.** For BraTS and ProstateX, segmentation results are shown from the region highlighted in the image (purple). Average DSC (%) and HD (mm) scores are mentioned at the top of each prediction. Our GeoLS minimizes classification errors in ambiguous regions, such as the non-enhancing core (blue) in BraTS, the pancreas (yellow) in FLARE, and PZ (blue) and AFS (yellow) zones in the ProstateX examples. Coloring denotes different tumor structures (top), abdominal organs (middle), and prostatic zones (bottom).

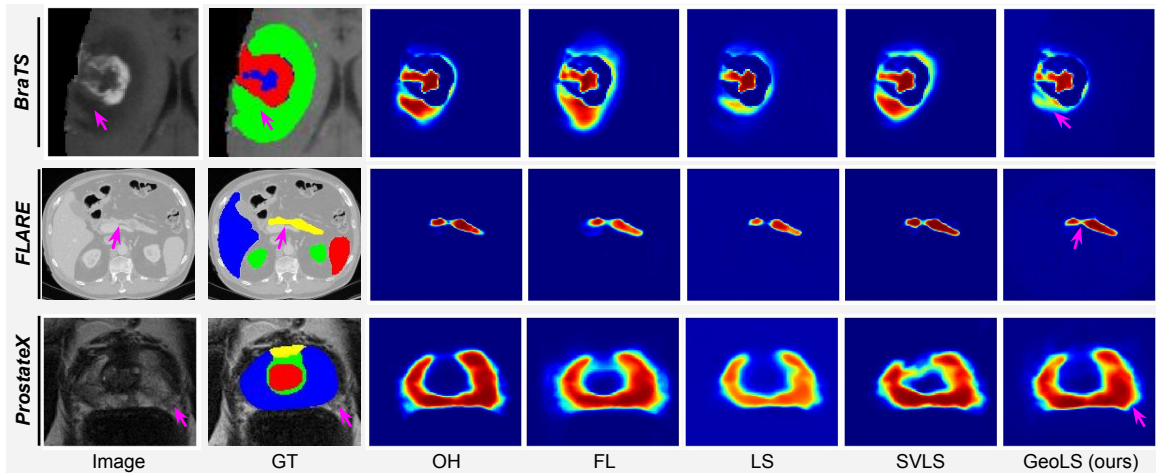


Figure 6: **Predicted probability maps.** The probability maps indicate a non-enhancing core (blue) in BraTS (top), a pancreas (yellow) in FLARE (middle), and a PZ (blue) in ProstateX (bottom), corresponding to the examples shown in the qualitative results. Our GeoLS yields reasonably low probabilities in poorly defined image intensities and misclassified regions while maintaining high probabilities in non-ambiguous regions.

345 segmentations are arguably challenging due to imprecise boundaries between different zones.
 346 In the bottom row, the results of prostatic zone segmentations are poor in all approaches.
 347 Our method produces reasonable segmentation results, notably in the AFS prostatic zone
 348 (yellow). In addition, the prediction probability maps of baselines and our method for the
 349 same examples are shown in Fig. 6. Our GeoLS produces reasonably low probabilities in
 350 poorly defined image intensities and misclassified regions, ensuring segmentation accuracy
 351 even in challenging areas. At the same time, it consistently maintains high probabilities
 352 in well-defined image intensity regions. Furthermore, the quantitative results presented in
 353 Sec. 4.4 support these visual results. These results indicate that supplying image gradient
 354 information through geodesic maps in our intensity-based soft-labeling approach enhances
 355 the segmentation performance.

356 4.6 Sensitivity to γ

357 The hyperparameter γ in Eq. 4 plays a crucial role in balancing between the Geodesic
 358 Distance and the Euclidean Distance. Since the intensity variations and spatial distance
 359 can influence the generalized geodesic distance transform, we investigate the segmentation
 360 performance by varying the γ parameter and report their results in Fig. 7, across all datasets.
 361 Additionally, we include the segmentation result obtained from a model trained with $\gamma = 0$,
 362 i.e., utilizing only the Euclidean Distance for soft labels. The results demonstrate that the
 363 segmentation performance is better for higher γ values compared to the models solely relying
 364 on Euclidean distance maps. This indicates that incorporating geodesic information based
 365 on image gradients in our soft labels positively impacts the performance of segmentation
 366 tasks.

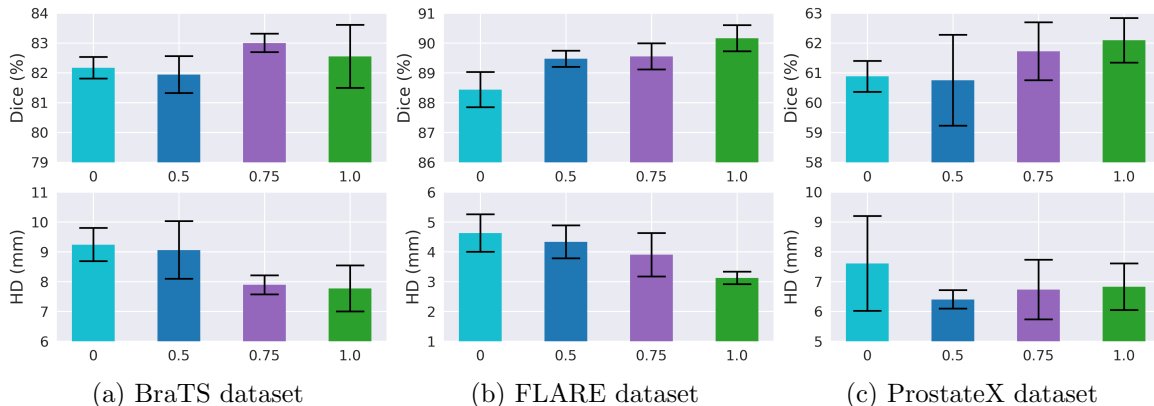


Figure 7: **Sensitivity of geodesic factor γ on segmentation performance** - Each bar indicates the average DSC \uparrow (top) and HD \downarrow (bottom) scores for BraTS, FLARE, and ProstateX datasets. $\gamma = 0$ here uses only using Euclidean Distance. Segmentation accuracy improves when the γ value is increased towards 1, indicating a higher emphasis on Geodesic Distance in soft labels.

Table 4: **Performance under different seed sets \mathcal{S}** . Average DSC and HD scores on BraTS, FLARE, and ProstateX datasets are reported. Segmentation accuracy is consistent across datasets for skeleton-based seed points. The bold and underlined indicate the best and second-best results.

Datasets	BraTS		FLARE		ProstateX	
choice of \mathcal{S}	DSC (%) \uparrow	HD (mm) \downarrow	DSC (%) \uparrow	HD (mm) \downarrow	DSC (%) \uparrow	HD (mm) \downarrow
random-3	82.98 ± 0.68	8.10 ± 0.09	87.83 ± 1.02	4.79 ± 0.16	58.65 ± 3.73	7.41 ± 1.59
random-5	82.51 ± 0.80	9.00 ± 0.70	89.46 ± 1.00	4.20 ± 0.97	60.88 ± 0.85	7.07 ± 0.33
random-7	82.36 ± 0.48	8.89 ± 0.81	89.23 ± 0.21	4.41 ± 0.49	61.76 ± 2.62	6.84 ± 0.91
skeleton	83.00 ± 0.31	7.89 ± 0.32	90.16 ± 0.44	3.12 ± 0.21	62.09 ± 0.75	6.83 ± 0.78
erosion	81.93 ± 0.93	9.17 ± 0.68	89.56 ± 0.08	3.63 ± 0.27	61.72 ± 0.90	6.96 ± 0.55

367 4.7 Choice of seed set \mathcal{S}

368 Our soft label relies on the geodesic maps, which vary with the different choices of seed set \mathcal{S} .
 369 Therefore, to validate the effectiveness of our seeding strategy on segmentation performance,
 370 we conduct experiments with different seed-set strategies. These strategies involve obtaining
 371 a random selection of pixels within each target class. For this, our experiments include 3,
 372 5, and 7 randomly selected pixels as seed points. Such seed points are inadequate for large
 373 regions, such as the liver, or multiple instances of a class label, such as the kidney. To address
 374 this issue, seed sets are also obtained using the remainings of the skeletonization and erosion
 375 operations applied to each target class. The results of these experiments are reported in
 376 Table 4. It shows that the segmentation performances are comparable for different seed-set
 377 choices, which further demonstrates the strength of our geodesic soft labels. Furthermore,
 378 the results suggest that the skeleton-based seed strategy consistently yields favorable results
 379 across all datasets, which indicates that this seeding strategy could also be viable on new
 380 datasets.

381 4.8 Combination of loss functions

382 The main goal of this work is to provide an alternative to state-of-the-art soft labeling losses
 383 by leveraging geodesic distance transform. Nevertheless, the proposed approach is orthog-
 384 onal to other types of segmentation losses, including widely used Dice loss (Sudre et al.,
 385 2017). Moreover, combined CE and Dice losses are often employed to train segmentation
 386 models for medical images (Ma et al., 2021; Taghanaki et al., 2019). Thus, we investigate
 387 whether the findings observed when comparing the CE loss hold when we combine the
 388 proposed GeoLS with the Dice loss. These results, depicted in Fig. 8, demonstrate that
 389 adding the Dice loss improves the segmentation performance of both CE and GeoLS across
 390 all datasets. Moreover, combining GeoLS and Dice losses achieves the best results in most
 391 cases, demonstrating the consistency of our geodesic label-smoothing approach.

392 Furthermore, we performed experiments by combining our GeoLS with a boundary loss
 393 (BL) first and then with a focal loss (FL), and their results are reported in Fig. 9. The
 394 results show a similar trend as with a combination of Dice loss. Combining our method
 395 with the BL and FL yields better segmentation results compared to the CE combined with
 396 the BL and FL across all three datasets, in most cases. These results demonstrate the
 397 robustness of the proposed GeoLS when combined with other loss functions.

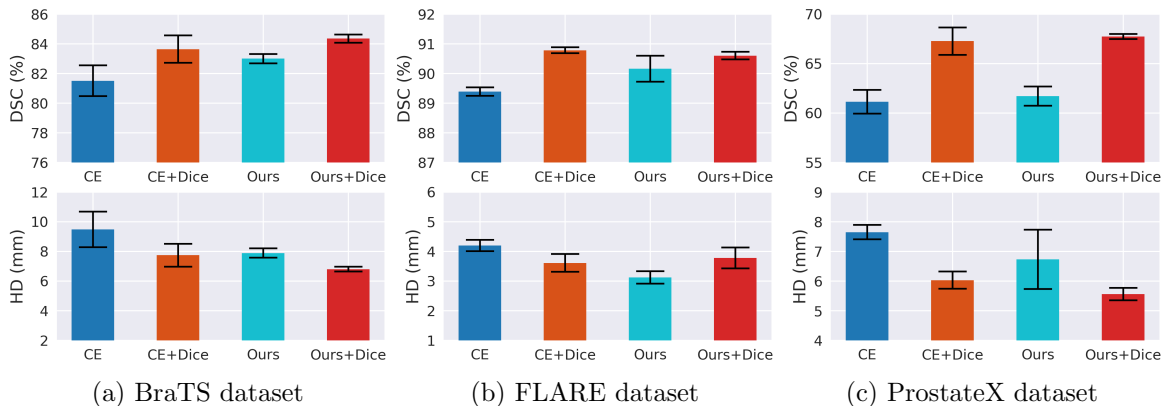


Figure 8: **Segmentation results with a combination of Dice loss** - Each bar indicates the average DSC \uparrow (top) and HD \downarrow (bottom) scores on all three datasets. The performance of segmentation improves by adding Dice loss on both CE and our models. Combination of Dice loss with our yields consistently best in most cases.

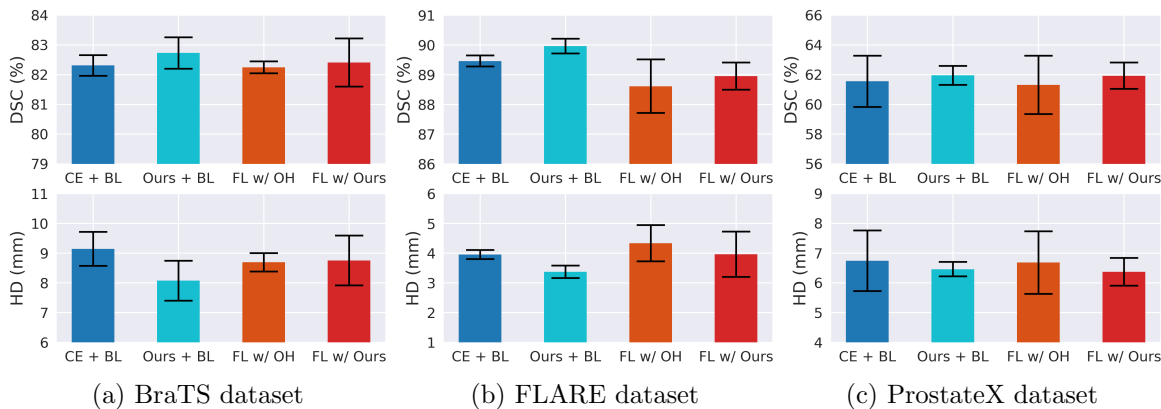


Figure 9: **Segmentation results with a combination of Boundary loss (BL) and Focal loss (FL)** - Each bar indicates the average DSC \uparrow (top) and HD \downarrow (bottom) scores on all three datasets. Combining our method with BL and FL consistently provides better segmentation results compared to CE combined with BL and FL in most cases.

398 5. Discussion and Conclusion

399 Despite the growing popularity of contemporary soft-labeling approaches, the underlying
 400 image context information associated with the label is largely overlooked in the soft labels
 401 for image segmentation. This work demonstrates that incorporating such information into
 402 standard hard labels would improve the performance of deep segmentation networks. To
 403 that effect, our contribution, a Geodesic label smoothing (GeoLS), incorporates intensity
 404 variation details into the soft-labeling process through geodesic distance transforms. More
 405 specifically, our proposed approach generates new intensity-based soft labels that capture
 406 ambiguity between neighboring target regions. Employing our soft labels in the training
 407 of segmentation models has consequently demonstrated an improved segmentation perfor-

408 mance. Our results have in fact shown that our geodesic-based smoothing consistently
409 outperforms state-of-the-art approaches in soft-labeling, across three different datasets:
410 multi-class tumor segmentation in brain MRIs, organ segmentation in abdominal CTs,
411 and zone segmentation in prostatic MR volumes. Both quantitative and qualitative results
412 indicate notable improvements in the segmentation of known challenging regions, such as
413 of enhancing tumors, as well as the pancreas.

414 Furthermore, the ablation study conducted on the geodesic factor parameter indicates
415 that our geodesic maps integrate richer intensity information in the yielded soft labels, ef-
416 fectively producing an improved segmentation performance than utilizing only Euclidean
417 distance maps. Our experiments have also evaluated several key seeding strategies for gen-
418 erating soft labels. These results show that the skeleton-based strategy remains consistent
419 across all datasets. The design of the seeding process can be further explored in order
420 to better capture the intrinsic structures of target objects. This work provides, therefore,
421 a valuable alternative to hard-labeling and existing soft-labeling losses. Nonetheless, our
422 geodesic label smoothing loss can also be combined with other segmentation losses, such as
423 the conventional Dice loss. The use of such loss has in fact shown further improvements
424 in the segmentation accuracy within our experiments. As future work, our approach could
425 also be potentially applicable to segmentation tasks under noisy annotations (Lukasik et al.,
426 2020; Karimi et al., 2023). Overall, our proposed geodesic-based soft-labeling could be vir-
427 tually leveraged in broader ranges of applications where annotation remains challenging due
428 to ambiguities in image intensities across regions.

429 **Acknowledgments**

430 This work has been funded by the Canada Research Chair on Shape Analysis in Medical
431 Imaging, the Natural Sciences and Engineering Research Council of Canada (NSERC), and
432 the Fonds de Recherche du Quebec (FQRNT). Special thanks to Mustafa Chasmai and
433 Kumar Devesh for their initial discussions on this work.

434 **Ethical Standards**

435 The work follows appropriate ethical standards in conducting research and writing the
436 manuscript, following all applicable laws and regulations regarding the treatment of animals
437 or human subjects.

438 **Conflicts of Interest**

439 The authors declare no known conflicts of interest in any personal relationship, financial
440 or otherwise, to disclose. The authors are affiliated with the Department of Computer and
441 Software Engineering at ETS Montreal, Montreal, Canada (etsmtl.ca), and Polytechnique
442 Montreal, Canada (polymtl.ca). Fundings are from government agencies (Canada Research
443 Chair, NSERC, FRQNT).

444 **Data availability**

445 All the datasets used in this research work are publicly available.

446 **References**

447 Sukesh Adiga Vasudeva, Jose Dolz, and Herve Lombaert. GeoLS: Geodesic label smoothing
448 for image segmentation. In *Medical Imaging with Deep Learning*, 2023.

449 Spyridon Bakas, Hamed Akbari, Aristeidis Sotiras, Michel Bilello, Martin Rozycki, Justin S
450 Kirby, John B Freymann, Keyvan Farahani, and Christos Davatzikos. Advancing the
451 cancer genome atlas glioma MRI collections with expert segmentation labels and radiomic
452 features. *Scientific data*, 4(1):1–13, 2017.

453 Spyridon Bakas, Mauricio Reyes, Andras Jakab, Stefan Bauer, Markus Rempfler, Alessan-
454 dro Crimi, Russell Takeshi Shinohara, Christoph Berger, Sung Min Ha, Martin Rozycki,
455 et al. Identifying the best machine learning algorithms for brain tumor segmentation,
456 progression assessment, and overall survival prediction in the BraTS challenge. *arXiv*
457 *preprint arXiv:1811.02629*, 2018.

458 Eric Baum and Frank Wilczek. Supervised learning of probability distributions by neural
459 networks. In *Neural information processing systems*, 1987.

460 Toan Duc Bui, Li Wang, Jian Chen, Weili Lin, Gang Li, and Dinggang Shen. Multi-
461 task learning for neonatal brain segmentation using 3D Dense-UNet with dense attention
462 guided by geodesic distance. In *Domain Adaptation and Representation Transfer and*
463 *Medical Image Learning with Less Labels and Imperfect Data - Medical Image Computing*
464 *and Computer Assisted Intervention Workshop*, pages 243–251. Springer, 2019.

465 Özgün Çiçek, Ahmed Abdulkadir, Soeren S Lienkamp, Thomas Brox, and Olaf Ronneberger.
466 3D U-Net: learning dense volumetric segmentation from sparse annotation. In *Medical*
467 *Image Computing and Computer-Assisted Intervention*, pages 424–432. Springer, 2016.

468 Antonio Criminisi, Toby Sharp, and Andrew Blake. GeoS: Geodesic image Segmentation.
469 In *European Conference on Computer Vision*, pages 99–112. Springer, 2008.

470 James S Duncan and Nicholas Ayache. Medical image analysis: Progress over two decades
471 and the challenges ahead. *Transactions on Pattern Analysis and Machine Intelligence*,
472 22(1):85–106, 2000.

473 Neamat El Gayar, Friedhelm Schwenker, and Günther Palm. A study of the robustness
474 of KNN classifiers trained using soft labels. In *Artificial Neural Networks in Pattern*
475 *Recognition IAPR Workshop*, pages 67–80. Springer, 2006.

476 Adrian Galdran, Jihed Chelbi, Riadh Kobi, José Dolz, Hervé Lombaert, Ismail Ben Ayed,
477 and Hadi Chakor. Non-uniform label smoothing for diabetic retinopathy grading from
478 retinal fundus images with deep neural networks. *Translational Vision Science & Tech-*
479 *nology*, 9(2):34–34, 2020.

- 480 Charley Gros, Andreeanne Lemay, and Julien Cohen-Adad. SoftSeg: advantages of soft
481 versus binary training for image segmentation. *Medical Image Analysis*, 71:102038, 2021.
- 482 Adam Hammoumi, Maxime Moreaud, Christophe Ducottet, and Sylvain Desroziers. Adding
483 geodesic information and stochastic patch-wise image prediction for small dataset learn-
484 ing. *Neurocomputing*, 456:481–491, 2021.
- 485 Robert M Hayward, Nicolas Patronas, Eva H Baker, Gilbert Vézina, Paul S Albert, and
486 Katherine E Warren. Inter-observer variability in the measurement of diffuse intrinsic
487 pontine gliomas. *Journal of neuro-oncology*, 90:57–61, 2008.
- 488 Kaiming He, Xiangyu Zhang, Shaoqing Ren, and Jian Sun. Deep residual learning for image
489 recognition. In *Computer Vision and Pattern Recognition*, pages 770–778. IEEE, 2016.
- 490 Xingxin He, Leyuan Fang, Hossein Rabbani, Xiangdong Chen, and Zhimin Liu. Retinal
491 Optical Coherence Tomography image classification with label smoothing generative ad-
492 versarial network. *Neurocomputing*, 405:37–47, 2020.
- 493 Mohammad Hesam Hesamian, Wenjing Jia, Xiangjian He, and Paul Kennedy. Deep learning
494 techniques for medical image segmentation: achievements and challenges. *Journal of*
495 *Digital Imaging*, 32(4):582–596, 2019.
- 496 Fabian Isensee, Paul F Jaeger, Simon AA Kohl, Jens Petersen, and Klaus H Maier-Hein.
497 nnU-Net: a self-configuring method for deep learning-based biomedical image segmenta-
498 tion. *Nature methods*, 18(2):203–211, 2021.
- 499 Mobarakol Islam and Ben Glocker. Spatially varying label smoothing: Capturing uncer-
500 tainty from expert annotations. In *Information Processing in Medical Imaging*, pages
501 677–688. Springer, 2021.
- 502 Mobarakol Islam, Lalithkumar Seenivasan, Lim Chwee Ming, and Hongliang Ren. Learning
503 and reasoning with the graph structure representation in robotic surgery. In *Medical*
504 *Image Computing and Computer-Assisted Intervention*, pages 627–636. Springer, 2020.
- 505 Leo Joskowicz, D Cohen, N Caplan, and Jacob Sosna. Inter-observer variability of manual
506 contour delineation of structures in CT. *European Radiology*, 29(3):1391–1399, 2019.
- 507 Davood Karimi, Caitlin K Rollins, Clemente Velasco-Annis, Abdelhakim Ouaalam, and Ali
508 Gholipour. Learning to segment fetal brain tissue from noisy annotations. *Medical Image*
509 *Analysis*, 85:102731, 2023.
- 510 Eytan Kats, Jacob Goldberger, and Hayit Greenspan. Soft labeling by distilling anatom-
511 ical knowledge for improved MS lesion segmentation. In *International Symposium on*
512 *Biomedical Imaging*, pages 1563–1566. IEEE, 2019.
- 513 James M Keller, Michael R Gray, and James A Givens. A fuzzy k-nearest neighbor algo-
514 rithm. *Transactions on Systems, Man, and Cybernetics*, (4):580–585, 1985.
- 515 DP Kingma and Jimmy Ba. Adam: a method for stochastic optimization. *International*
516 *Conference on Learning Representations*, 2015.

- 517 Peter Kontschieder, Pushmeet Kohli, Jamie Shotton, and Antonio Criminisi. GeoF:
518 Geodesic Forests for learning coupled predictors. In *Computer Vision and Pattern Recognition*, pages 65–72. IEEE, 2013.
519
- 520 Tsung-Yi Lin, Priya Goyal, Ross Girshick, Kaiming He, and Piotr Dollár. Focal loss for
521 dense object detection. In *International Conference on Computer Vision*, pages 2980–
522 2988. IEEE, 2017.
- 523 Geert Litjens, Oscar Debats, Jelle Barentsz, Nico Karssemeijer, and Henkjan Huisman.
524 Computer-aided detection of prostate cancer in MRI. *Transactions on Medical Imaging*,
525 33(5):1083–1092, 2014.
- 526 Geert Litjens, Thijs Kooi, Babak Ehteshami Bejnordi, Arnaud Arindra Adiyoso Setio,
527 Francesco Ciompi, Mohsen Ghafoorian, Jeroen Awm Van Der Laak, Bram Van Ginneken,
528 and Clara I Sánchez. A survey on deep learning in medical image analysis. *Medical Image*
529 *Analysis*, 42:60–88, 2017.
- 530 Joao Lourenço-Silva and Arlindo L Oliveira. Using soft labels to model uncertainty in
531 medical image segmentation. In *Medical Image Computing and Computer Assisted Inter-*
532 *vention - Brainlesion Workshop*, pages 585–596. Springer, 2021.
- 533 Michal Lukasik, Srinadh Bhojanapalli, Aditya Menon, and Sanjiv Kumar. Does label
534 smoothing mitigate label noise? In *International Conference on Machine Learning*, pages
535 6448–6458. PMLR, 2020.
- 536 Tohar Lukov, Na Zhao, Gim Hee Lee, and Ser-Nam Lim. Teaching with soft label smoothing
537 for mitigating noisy labels in facial expressions. In *European Conference on Computer*
538 *Vision*, pages 648–665. Springer, 2022.
- 539 Jun Ma, Jianan Chen, Matthew Ng, Rui Huang, Yu Li, Chen Li, Xiaoping Yang, and
540 Anne L Martel. Loss odyssey in medical image segmentation. *Medical Image Analysis*,
541 71:102035, 2021.
- 542 Jun Ma, Yao Zhang, Song Gu, Xingle An, Zhihe Wang, Cheng Ge, Congcong Wang, Fan
543 Zhang, Yu Wang, Yinan Xu, et al. Fast and Low-GPU-memory Abdomen CT organ
544 sEgmentation: The FLARE challenge. *Medical Image Analysis*, 82:102616, 2022.
- 545 Bjoern H Menze, Andras Jakab, Stefan Bauer, Jayashree Kalpathy-Cramer, Keyvan Fara-
546 hani, Justin Kirby, Yuliya Burren, Nicole Porz, Johannes Slotboom, Roland Wiest, et al.
547 The multimodal brain tumor image segmentation benchmark (BraTS). *Transactions on*
548 *Medical Imaging*, 34(10):1993–2024, 2014.
- 549 Rafael Müller, Simon Kornblith, and Geoffrey E Hinton. When does label smoothing help?
550 *Advances in Neural Information Processing Systems*, 32, 2019.
- 551 Dzung L Pham, Chenyang Xu, and Jerry L Prince. Current methods in medical image
552 segmentation. *Annual Review of Biomedical Engineering*, 2(1):315–337, 2000.
- 553 Alexis Protiere and Guillermo Sapiro. Interactive image segmentation via adaptive weighted
554 distances. *Transactions on Image Processing*, 16(4):1046–1057, 2007.

- 555 Wu Qiu, Jing Yuan, Martin Rajchl, Jessica Kishimoto, Yimin Chen, Sandrine de Rib-
 556 aupierre, Bernard Chiu, and Aaron Fenster. 3D MR ventricle segmentation in pre-term
 557 infants with post-hemorrhagic ventricle dilatation (PHVD) using multi-phase geodesic
 558 level-sets. *NeuroImage*, 118:13–25, 2015.
- 559 Reuven Y Rubinstein and Dirk P Kroese. *The cross-entropy method: a unified approach to*
 560 *combinatorial optimization, Monte-Carlo simulation, and machine learning*, volume 133.
 561 Springer, 2004.
- 562 Sambu Seo, Mathias Bode, and Klaus Obermayer. Soft nearest prototype classification.
 563 *Transactions on Neural Networks*, 14(2):390–398, 2003.
- 564 Carole H Sudre, Wenqi Li, Tom Vercauteren, Sebastien Ourselin, and M Jorge Cardoso.
 565 Generalised Dice overlap as a deep learning loss function for highly unbalanced segmenta-
 566 tions. In *Deep Learning in Medical Image Analysis and Multimodal Learning for Clinical*
 567 *Decision Support*, pages 240–248. Springer, 2017.
- 568 Paul Suetens. *Fundamentals of medical imaging*. Cambridge University Press, 2017.
- 569 Christian Szegedy, Vincent Vanhoucke, Sergey Ioffe, Jon Shlens, and Zbigniew Wojna.
 570 Rethinking the inception architecture for computer vision. In *Computer Vision and*
 571 *Pattern Recognition*, pages 2818–2826. IEEE, 2016.
- 572 Christian Szegedy, Sergey Ioffe, Vincent Vanhoucke, and Alexander Alemi. Inception-v4,
 573 Inception-ResNet and the impact of residual connections on learning. In *Association for*
 574 *the Advancement of Artificial Intelligence*, volume 31, 2017.
- 575 Saeid Asgari Taghanaki, Yefeng Zheng, S Kevin Zhou, Bogdan Georgescu, Puneet Sharma,
 576 Daguang Xu, Dorin Comaniciu, and Ghassan Hamarneh. Combo loss: Handling input
 577 and output imbalance in multi-organ segmentation. *Computerized Medical Imaging and*
 578 *Graphics*, 75:24–33, 2019.
- 579 Pin Tang, Pinli Yang, Dong Nie, Xi Wu, Jiliu Zhou, and Yan Wang. Unified medical image
 580 segmentation by learning from uncertainty in an end-to-end manner. *Knowledge-Based*
 581 *Systems*, 241:108215, 2022.
- 582 Pekka J Toivanen. New geodesic distance transforms for gray-scale images. *Pattern Recog-*
 583 *niton Letters*, 17(5):437–450, 1996.
- 584 Guotai Wang, Maria A Zuluaga, Wenqi Li, Rosalind Pratt, Premal A Patel, Michael Aert-
 585 sen, Tom Doel, Anna L David, Jan Deprest, Sébastien Ourselin, et al. DeepIGeoS: a deep
 586 interactive geodesic framework for medical image segmentation. *Transactions on Pattern*
 587 *Analysis and Machine Intelligence*, 41(7):1559–1572, 2018.
- 588 Lin Wang, Xiufen Ye, Lie Ju, Wanji He, Donghao Zhang, Xin Wang, Yelin Huang, Wei
 589 Feng, Kaimin Song, and Zongyuan Ge. Medical matting: Medical image segmentation
 590 with uncertainty from the matting perspective. *Computers in Biology and Medicine*, 158:
 591 106714, 2023.

- 592 Zehan Wang, Kanwal K Bhatia, Ben Glocker, Antonio Marvao, Tim Dawes, Kazunari
593 Misawa, Kensaku Mori, and Daniel Rueckert. Geodesic patch-based segmentation. In
594 *Medical Image Computing and Computer-Assisted Intervention*, pages 666–673. Springer,
595 2014.
- 596 Jie Wei, Zhengwang Wu, Li Wang, Toan Duc Bui, Liangqiong Qu, Pew-Thian Yap, Yong
597 Xia, Gang Li, and Dinggang Shen. A cascaded nested network for 3T brain MR image
598 segmentation guided by 7T labeling. *Pattern Recognition*, 124:108420, 2022.
- 599 Jie Ying, Wei Huang, Le Fu, Haima Yang, and Jiangzihao Cheng. Weakly supervised
600 segmentation of uterus by scribble labeling on endometrial cancer MR images. *Computers
601 in Biology and Medicine*, 167:107582, 2023.
- 602 Chang-Bin Zhang, Peng-Tao Jiang, Qibin Hou, Yunchao Wei, Qi Han, Zhen Li, and Ming-
603 Ming Cheng. Delving deep into label smoothing. *Transactions on Image Processing*, 30:
604 5984–5996, 2021.
- 605 S Kevin Zhou, Daniel Rueckert, and Gabor Fichtinger. *Handbook of medical image com-
606 puting and computer assisted intervention*. Academic Press, 2019.